

Research Paper

Structural and electronic properties of functionalized armchair and zigzag hexagonal silicon carbide: Insights for pyridine sensing applications

Nahed H. Teleb^{a,d,*}, Mahmoud A.S. Sakr^{b,*}, Mohamed A. Saad^b, Omar H. Abd-Elkader^c, Hazem Abdelsalam^{d,e}, Qinfang Zhang^{d,*}

^a Electron Microscope and Thin Films Department, National Research Centre, El-Buhouth Str., 12622, Dokki, Giza, Egypt

^b Center of Basic Science (CBS), Misr University of Science and Technology (MUST), 6th October City, Egypt

^c Department of Physics and Astronomy, College of Science, King Saud University, P.O. Box 2455, Riyadh 11451, Saudi Arabia

^d School of Materials Science and Engineering, Yancheng Institute of Technology, Yancheng 224051, PR China

^e Theoretical Physics Department, National Research Centre, El-Buhouth Str., 12622, Dokki, Giza, Egypt



ARTICLE INFO

Keywords:

Silicon carbide
Functionalization
Adsorption
Sensor
Electronic properties
Optical properties
Density functional theory

ABSTRACT

This study investigates the potential of functionalized armchair-edged hexagonal silicon carbide (AHSiC) and zigzag-edged hexagonal silicon carbide (ZHSiC) for sensor applications. We explored the structural, electronic, and adsorption properties of these materials after functionalization with CHO and COOH groups. Our findings reveal that functionalization significantly enhances the binding energy, with surface-COOH-functionalized ZHSiC exhibiting a 3.88 % improvement in binding energy compared to its non-functionalized counterpart, leading to improved stability. Additionally, functionalization modulates the electronic structure, influencing the optical properties and enhancing sensor performance. The adsorption of pyridine molecules on these surfaces was analyzed, demonstrating strong chemisorption for COOH-functionalized ZHSiC, particularly at the surface sites. The recovery time of adsorbed pyridine molecules was also significantly reduced by functionalization, with surface-COOH-functionalized ZHSiC achieving a recovery time as low as 2.22 ns at optimal adsorption sites.

1. Introduction

Pyridine is a significant chemical compound extensively utilized as an organic reagent and a precursor in the production of various products, including insecticides, pesticides, herbicides, pharmaceuticals, dyes, fragrances, rubber additives, animal feed additives, and adhesives, among others. However, due to its volatile nature, pyridine can be readily released into the environment during these synthetic processes. Exposure to pyridine, whether by inhalation, ingestion, or skin absorption, poses health risks and can lead to pyridine poisoning symptoms such as headaches, coughing, respiratory distress, laryngitis, nausea, and vomiting. Consequently, it is crucial to develop a method that is straightforward, sensitive, and accurate for detecting pyridine concentrations. To date, various techniques have been devised to detect pyridine, including fluorometric and colorimetric detection [1–4], optical fiber sensors [5], gas chromatography (GC) [6,7], liquid chromatography-mass spectrometry (LC-MS) [8], gas chromatography-mass spectrometry

* Corresponding authors.

E-mail addresses: n_sleam@yahoo.com (N.H. Teleb), mahmoud.sakr@must.edu.eg (M.A.S. Sakr), qfangzhang@gmail.com (Q. Zhang).

<https://doi.org/10.1016/j.cjph.2025.01.008>

Received 14 November 2024; Received in revised form 31 December 2024; Accepted 6 January 2025

Available online 7 January 2025

0577-9073/© 2025 The Physical Society of the Republic of China (Taiwan). Published by Elsevier B.V. All rights are reserved, including those for text and data mining, AI training, and similar technologies.

(GC–MS) [9], electric field-assisted liquid-phase microextraction [10], and potentiometric sensors [11].

Traditional methods for detecting and analyzing pyridine derivatives, such as gas chromatography (GC) and optical sensors, have been widely used due to their well-established reliability. However, these techniques have limitations in terms of sensitivity, response time, and operational complexity. For instance, gas chromatography requires extensive sample preparation, long analysis times, and expensive equipment, which limits its use for real-time or on-site detection [12]. Optical sensors, although faster, often suffer from lower sensitivity and selectivity, particularly in complex environments with multiple analytes, which can interfere with detection [13]. In contrast, the functionalized SiC nanostructures explored in this study offer significant advantages. The functionalization of hexagonal silicon carbide (SiC) with groups like CHO and COOH enhances the material's adsorption properties, leading to stronger chemisorption of the target molecules such as pyridine. This characteristic allows for extremely sensitive detection with fast response and recovery times, positioning functionalized SiC-based sensors as a promising solution for real-time monitoring. Additionally, functionalization modifies the electronic and optical properties of SiC surfaces, offering opportunities to design sensors that leverage both adsorption behavior and optical signal variations. This dual sensitivity—along with the simplicity of sensor design and potential for miniaturization makes SiC sensors a viable alternative to conventional methods, especially in applications requiring rapid and on-site detection.

Two-dimensional (2D) materials [14] have attracted immense interest due to their remarkable physical and chemical properties, making them leading candidates for next-generation technological advancements [15–18]. These materials, which are extremely thin and lightweight, exist in single layers like graphene [19], SiC [20,21], silicene [22], transition metal dichalcogenides (TMDs) [23], and MXenes [24–27], as well as in few-layered forms, including layered graphene [20], phosphorene [28], and various heterostructures [29]. The distinctive features of these materials open doors to a wide array of applications in fields such as electronics [30,31], optoelectronics [32], spintronics [33,34], quantum computing [35], sensors [36], catalysis [37], energy storage [38], and photovoltaics [39,40], and biological applications [41].

Two-dimensional quantum dots (2D-QDs), a subset of 2D materials with sizes typically under 20 nm, possess unique properties shaped by their size and edge configurations [42]. These nanodots provide unparalleled control over electronic and optical properties, with the flexibility to modify these characteristics through adjustments in size, edge termination, and chemical functionalization. Notably, as the size of a quantum dot diminishes, the electronic and optical energy gap expands [43–46]. Chemical modifications, including doping [30], vacancy introduction [47–49], and the attachment of chemical groups [47], further broaden the application potential of 2D-QDs, allowing for tailored physical and chemical properties. For instance, hexagonal boron nitride (hBN) quantum dots, when chemically modified, demonstrate remarkable metal ion detection abilities, showing enhanced adsorption energies compared to unmodified nanodots [50]. Quantum dots derived from materials like graphene, phosphorene, TMDs, and MXenes, especially when chemically altered, have also received significant attention for applications in pollutant sensing and removal [51–55]. Their abundance of active sites, large specific surface area, engineered energy gaps, superior photo-trapping capabilities, and capacity for multi-exciton generation position 2D-QDs as promising candidates in catalytic applications [56]. This study explores functionalized hexagonal silicon carbide (SiC) nanostructures—armchair (AHSiC) and zigzag (ZHSiC)—for sensor applications. Functionalizing SiC with CHO and COOH groups enhances binding energy and stability while modulating electronic and optical properties. Pyridine adsorption on these surfaces reveals strong chemisorption, especially for COOH-functionalized ZHSiC at surface sites, with recovery times depending on the functional group and site. These findings highlight the potential of functionalized SiC nanostructures for sensors leveraging tailored optical responses and selective adsorption.

2. Computational methodology

The structural optimization, electronic properties (HOMO-LUMO), Mulliken charge, and optical properties of the studied structures were investigated using density functional theory (DFT) as implemented in Gaussian 16 [57,58]. To accurately capture electronic and optical properties, the hybrid B3LYP functional [59] was applied, known for its reliable results in similar materials. The 6-31G basis set was selected for its balance of computational efficiency and accuracy [60], making it widely adopted in related studies [50,61–63]. Optical properties were further evaluated using time-dependent DFT calculations, focusing on the first fifty excited states to provide insights into the system's photophysical behavior. While computational-only approaches offer valuable insights, they come with inherent limitations, including model accuracy, parameter sensitivity, and computational cost. Therefore, it is essential to conduct experimental tests to validate the significant results presented in this study.

3. Results and discussions

3.1. Pristine and functionalized derivatives structures

In this section, we explore the structural parameters, stability, electronic properties, and Mulliken charge distribution of AHSiC and ZHSiC, along with their functionalized derivatives. The investigation provides insights into the impact of functionalization on the physical and chemical properties of these materials.

3.1.1. Optimized structures

The optimized structures of armchair-edged hexagonal silicon carbide (AHSiC) and zigzag-edged hexagonal silicon carbide (ZHSiC) were analyzed, focusing on two key functionalization sites: the edge (e) and the surface (s) (Fig. 1a, b). The functionalization sites were carefully selected at the edge (e) and surface (s) of the structures to explore the distinct effects on chemical reactivity. The edge sites are

highly reactive due to the unsaturated bonds, which allow for significant alterations in electronic and chemical properties upon functionalization. Surface sites, on the other hand, are more stable but offer opportunities for modifying the material's interaction with its environment. By replacing hydrogen atoms at the edge with CHO and COOH groups, we can introduce polar functionalities that enhance reactivity and adsorption capabilities while functionalizing the surface with similar groups increases interaction potential without significantly destabilizing the structure. This dual-site approach and surface—offers insights into optimizing SiC for applications requiring controlled surface chemistry and enhanced performance in catalysis, sensing, and electronic devices. The color-coded representation of the atoms and functional groups in the figure visually highlights the spatial arrangement and structural modifications.

The optimized structures of AHSiC and ZHSiC were analyzed, focusing on key quantum parameters such as bond lengths, bond angles, dihedral angles, and binding energy (BE), as presented in Table 1. The bond lengths between carbon and silicon atoms (C1-Si2 and C3-Si4) remain stable across the various structures, with values ranging from 1.79 to 1.84 Å. These small variations suggest that the introduction of functional groups, such as CHO and COOH, does not significantly alter the backbone of the SiC lattice, preserving its structural integrity. The bond angles (C1-Si2-C3) across the compounds range from 119.94° to 120.65°, which corresponds to a perfect trigonal planar geometry. This indicates that the carbon atoms involved in bonding are mostly sp² hybridized, as bond angles close to 120° are characteristic of sp² hybridization. In this configuration, the carbon atoms form three sigma bonds with adjacent atoms in the SiC structure, while the remaining unhybridized p orbital contributes to the π-bonding within the planar hexagonal network. The dihedral angles (C1-Si2-C3-Si4) remain close to 180°, indicating a mostly planar structure. However, small deviations, particularly in surface-functionalized compounds (e.g., AHSiC-s-CHO and ZHSiC-s-COOH), reflect some degree of structural twisting caused by the addition of functional groups.

3.1.2. Stability investigations

The structure stability of AHSiC and ZHSiC and its based materials were investigated using the binding energy (BE), calculated using the formula:

$$BE = \frac{E_C N_C + E_H N_H + E_O N_O - E_t}{N_t}$$

Where E_C , E_H , E_O , and E_t represent the energy of carbon atoms, hydrogen atoms, oxygen atoms, and the total energy of the nanotube, respectively. N_C , N_H , N_O , and N_t denote the number of carbon atoms, hydrogen atoms, oxygen atoms, and the total number of atoms in the structure, respectively.

The BE of AHSiC and ZHSiC were significantly influenced by the addition of functional groups such as CHO and COOH. Functionalization not only impacts the stability of the material but also affects its electronic properties, making these modified structures suitable for various applications such as catalysis and sensing. As indicated in Table 1, the addition of CHO and COOH groups leads to subtle changes in the BE across both AHSiC and ZHSiC configurations, but these effects vary depending on the position of the functionalization (e or s) and the type of functional group.

For AHSiC, the introduction of CHO and COOH at both e and s positions results in a slight increase in BE, though the magnitude of this change depends on the specific functional group and site of attachment. For instance, the BE of AHSiC increased from 5.216 eV to 5.295 eV with CHO functionalization at the e (AHSiC-e-CHO), indicating an improvement in stability due to the edge interactions. A

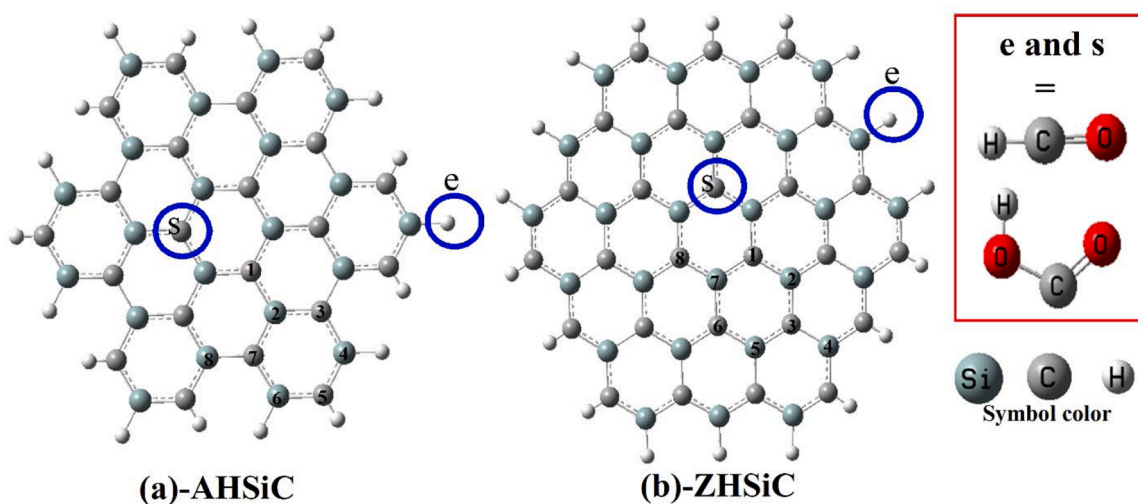


Fig. 1. (a, b) Optimized structures of AHSiC and ZHSiC, showing the selected sites e and s where functionalization occurs. At position e, the H atom is replaced by CHO and COOH functional groups, while at position s, the functional group is attached above the surface. The color-coded symbols representing atoms and the functional groups are provided on the right side of the figure.

Table 1

Some important quantum parameters like bond length (Å), dihedral, bond angles (degrees), and binding energy (BE) for AHSiC and ZHSiC and its based materials.

Compounds	C1-Si2	C3-Si4	C1-Si2-C3	C1-Si2-C3-Si4	BE (eV)
AHSiC	1.82	1.80	120.37	180.00	5.216
ZHSiC	1.82	1.83	120.06	180.00	5.425
AHSiC-e-CHO	1.82	1.79	120.58	179.97	5.295
AHSiC-s-CHO	1.82	1.79	120.31	177.72	5.228
AHSiC-e-COOH	1.82	1.80	120.34	180.00	5.326
AHSiC-s-COOH	1.81	1.79	120.65	179.15	5.261
ZHSiC-e-CHO	1.82	1.83	119.99	180.00	5.479
ZHSiC-s-CHO	1.81	1.83	120.10	177.97	5.428
ZHSiC-e-COOH	1.82	1.83	119.99	179.49	5.504
ZHSiC-s-COOH	1.83	1.84	119.94	177.92	5.449

similar trend is observed for COOH functionalization at the e (AHSiC-e-COOH), where the BE increases to 5.326 eV. However, s functionalization leads to smaller changes in BE, as seen in AHSiC-s-CHO (5.228 eV) and AHSiC-s-COOH (5.261 eV). These results suggest that e-functionalization has a more pronounced effect on the stability of AHSiC compared to s-functionalization. For ZHSiC, a more substantial effect is observed. ZHSiC is already more stable than AHSiC due to its intrinsic structural properties and shows an even greater increase in BE upon functionalization. For example, ZHSiC-e-CHO exhibits a BE of 5.479 eV, while ZHSiC-s-CHO has a slightly lower BE of 5.428 eV. COOH functionalization, especially at the edge (ZHSiC-e-COOH), results in the highest binding energy across all configurations, reaching 5.504 eV, underscoring the strong interaction between COOH and the zigzag-edged structure. Surface functionalization (ZHSiC-s-COOH) also increases the BE to 5.449 eV, though to a lesser extent than edge functionalization.

The difference between e- and s-functionalization is crucial in understanding how functional groups interact with the SiC structure. Functionalization at the edge typically leads to stronger BEs due to the presence of dangling bonds and undercoordinated atoms, which can form stronger interactions with the functional groups. Surface functionalization, while still enhancing stability, results in smaller increases in BE, as the interaction is more spread out and less localized. In summary, the addition of CHO and COOH functional groups enhances the BE of both AHSiC and ZHSiC, with the most significant increase observed in e-functionalized ZHSiC. These results highlight the importance of both the type of functional group and its position as e-functionalization with COOH leads to the highest stability, making ZHSiC-e-COOH a highly promising candidate for applications requiring stable and reactive surfaces. This effect is clearly reflected in the BE trends presented in Table 1.

3.1.3. Electronic study

In the analysis of the highest occupied molecular orbital/ lowest unoccupied molecular orbital (HOMO/LUMO) distributions for AHSiC, ZHSiC, and their functionalized derivatives (Fig. 2), orbital localization plays a crucial role in determining the materials' electronic properties. For AHSiC, the HOMO and LUMO are localized on Si and C, influencing the material's stability and interactions. Functionalization with CHO and COOH groups alters this behavior: in AHSiC-e-CHO, the CHO group significantly participates in the LUMO, enhancing electron-accepting properties, while in AHSiC-s-COOH, the COOH group contributes to the HOMO, boosting electron-donating behavior. In ZHSiC, similar localization patterns are observed. Functional groups also shift the electronic behavior: ZHSiC-s-CHO enhances electron donation via HOMO participation, while edge-attached CHO in ZHSiC-e-CHO contributes to electron acceptance. Functionalization at the surface enhances electron donation, while edge functionalization promotes electron acceptance. This tunability in HOMO/LUMO distribution indicates potential applications in electronics and catalysis, where controlled electron transfer is key.

Energy level analysis (Fig. 2) provides valuable insights into the electronic properties of AHSiC, ZHSiC, and their functionalized derivatives, especially for applications in sensing. For pristine AHSiC, the HOMO and LUMO energy levels are -5.162 eV and -2.004 eV, resulting in an energy gap (E_g) of 3.158 eV, indicating semiconducting behavior with moderate conductivity. In comparison, ZHSiC shows slightly enhanced conductivity with a smaller gap of 2.786 eV, attributed to its HOMO at -4.991 eV and LUMO at -2.204 eV. Upon functionalization, significant shifts in energy levels and gaps are observed, highlighting the impact of CHO and COOH groups on the materials' electronic structures. For AHSiC-e-CHO, the E_g reduces to 3.104 eV (HOMO: -5.307 eV, LUMO: -2.203 eV), reflecting a slight improvement in conductivity compared to pristine AHSiC. Surface functionalization with CHO (AHSiC-s-CHO) further reduces the gap to 2.984 eV, indicating enhanced electrical properties. This reduction in E_g suggests that CHO functionalization promotes electron transfer, making the material more sensitive to external stimuli, a key feature for sensing applications. For AHSiC functionalized with COOH, a similar trend is observed. In AHSiC-e-COOH, the gap remains unchanged at 3.154 eV, suggesting that edge functionalization with COOH has a minimal effect on conductivity. However, surface-functionalized AHSiC-s-COOH exhibits a reduced gap of 2.927 eV, reinforcing the idea that surface functionalization more effectively enhances the material's electrical response. These shifts indicate that functionalization with electron-donating groups like COOH can modulate the electronic structure, especially when positioned on the surface, making the material more responsive to environmental changes.

For ZHSiC and its derivatives, functionalization leads to even more pronounced changes in energy gaps. ZHSiC-e-CHO shows a significant reduction in E_g to 2.106 eV, reflecting a marked increase in conductivity compared to pristine ZHSiC. ZHSiC-s-CHO further decreases the gap to 1.589 eV, indicating exceptional conductivity and sensitivity, making it ideal for fast, responsive sensing applications. Similarly, ZHSiC-e-COOH and ZHSiC-s-COOH exhibit reduced E_g of 2.545 eV and 1.521 eV, respectively, underscoring the

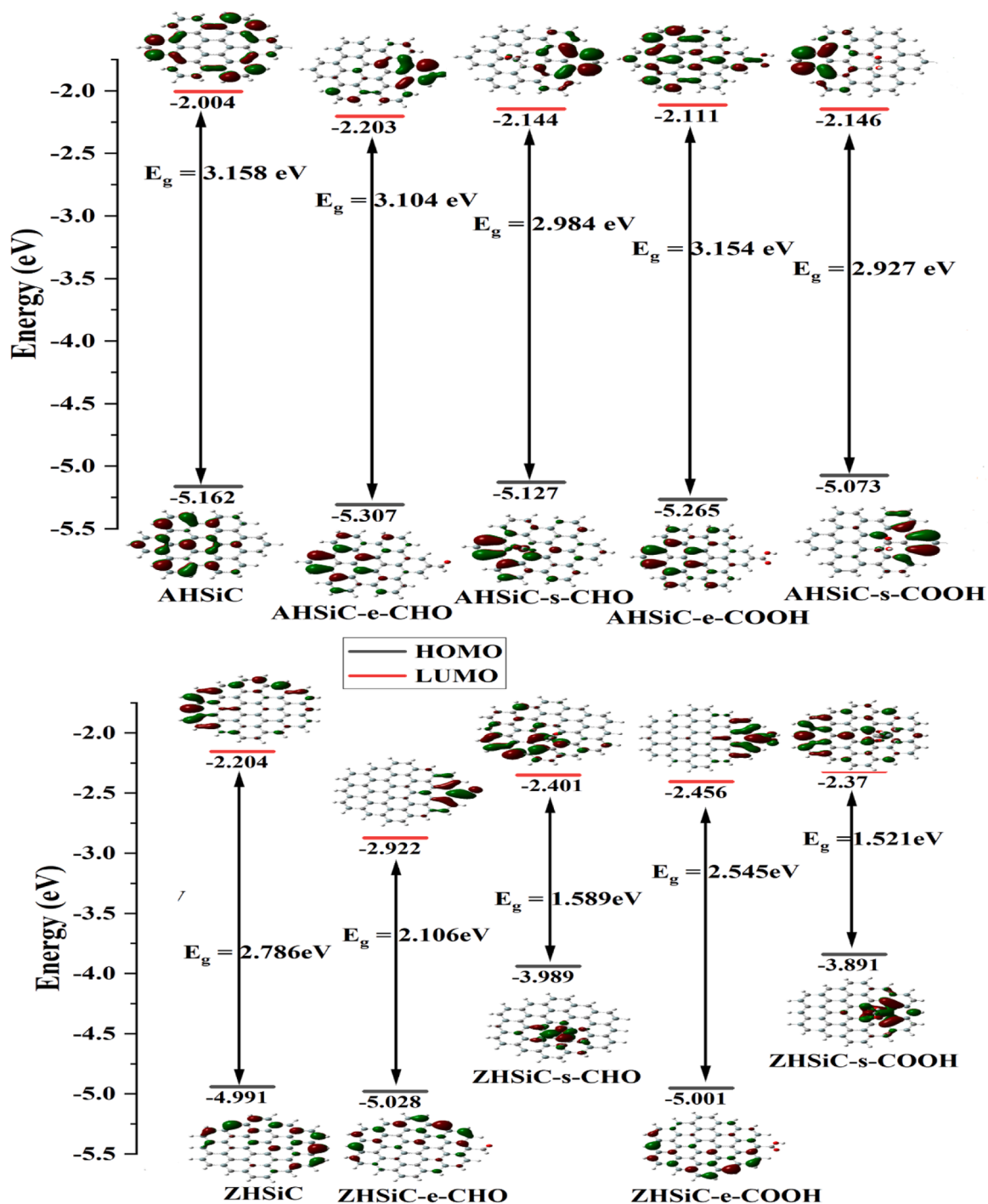


Fig. 2. HOMO/LUMO representations and energy levels of functionalized AHSiC and ZHSiC nanostructures, along with the corresponding energy gap (E_g).

role of COOH in tuning electronic properties, particularly in surface-functionalized configurations. The overall reduction in energy gaps upon functionalization—especially with surface-attached CHO and COOH groups—enhances the conductivity of both AHSiC and ZHSiC, making them more responsive to environmental changes. This tunability is crucial for developing extremely sensitive sensing devices, where the material's ability to detect small fluctuations in molecular or chemical environments is critical. By lowering the energy gap and modulating electron-donating or accepting properties, functionalized AHSiC and ZHSiC become excellent candidates for next-generation sensing technologies, offering precise control over electron transfer and high sensitivity to external stimuli.

3.1.4. Mulliken charge study

The Mulliken charge distribution and values for AHSiC, ZHSiC, and their derivatives indicate significant variations in charge distribution, which are important for their potential use as sensors. The red color on the C and O atoms in the carbonyl (CO) group signifies regions of negative charge, as shown in Fig. 3(a-j). For AHSiC and ZHSiC functionalized with –CHO and –COOH groups, the oxygen atoms in these functional groups carry significant negative charges (ranging from -0.34 to -0.58 for O, as detailed in Table 2). This negative charge increases the reactivity of these sites, making them more likely to interact with positively charged or electron-deficient species, a key feature for sensor applications. When target analytes come near these negatively charged sites, interactions such as charge transfer or electrostatic attraction can occur, leading to detectable changes in the electronic properties of the material. For the C1 atoms, there are notable negative charges across different compounds, especially in ZHSiC (ranging from -1.00 to -1.01, as shown in Table 2). These highly negative charges indicate that carbon sites are also reactive and can facilitate charge transfer events when exposed to analytes, further contributing to the sensor mechanism.

The green color on the Si atoms (Si2 and Si3) indicates regions of positive charge, with Mulliken charge values ranging from 0.77 to 1.27. These positively charged silicon atoms act as electron acceptors, playing a significant role in sensing processes. The variation in positive charge, particularly between Si2 and Si3 across different functionalized compounds, suggests that these atoms are sensitive to environmental changes, such as the presence of analytes or gases, potentially altering the material's electronic structure or conductivity. Fig. 3(k) displays the color scale, where red corresponds to regions of negative charge and green indicates regions of positive charge. This color coding effectively highlights the reactive sites in the materials and aids in visualizing their potential interactions with target analytes. The symbols and labels used to represent AHSiC and its derivatives are shown in Fig. 3a while those for ZHSiC and its derivatives are displayed in Fig. 3f. These notations provide clear distinctions between the two material families, allowing for a comparative analysis of their charge distribution and potential sensor capabilities.

In combination, the negatively charged carbon and oxygen atoms, and the positively charged silicon atoms form a reactive system capable of detecting environmental changes. The negatively charged regions can interact with electron-donating species, while the positively charged silicon atoms can accept electrons from nearby electron-rich species. These interactions result in measurable changes in the electronic properties, making AHSiC, ZHSiC, and their derivatives strong candidates for sensor applications. The functionalization with –CHO and –COOH groups enhances these properties by providing additional reactive sites for interacting with specific analytes, increasing the material's selectivity and sensitivity as a sensor.

3.2. Sensor applications

Here, we investigate the adsorption energy, recovery time, and electronic properties of AHSiC and ZHSiC, as well as their functionalized derivatives, following the adsorption of a single pyridine molecule.

3.2.1. Adsorption energy and type of adsorption

We chose AHSiC, AHSiC-e-CHO, AHSiC-s-CHO, and ZHSiC as representative structures from the broader set of studied molecules to provide a clear and comparative overview of adsorption behavior, as shown in Fig. 4 (a-f). These specific structures highlight key functionalization (–CHO group at e and s) and structural variations, offering insights into how different active sites (e vs. s) influence the interaction with the pyridine (Pyr) molecule. By focusing on these configurations, we can effectively illustrate the positions where adsorption occurs and demonstrate how both the functional group placement and structural differences impact adsorption characteristics.

The adsorption energies (E_a) of the complexes, as listed in Table 3, indicate the strength and nature of the interaction between pyridine and both AHSiC and ZHSiC. Based on the magnitude of the E_a , we can infer whether the interaction is physisorption (characterized by weaker van der Waals forces and low adsorption energies, typically below -0.5 eV) or chemisorption (stronger chemical bonds with adsorption energies greater than -0.5 eV). For pristine AHSiC, both AHSiC-s-Pyr and AHSiC-e-Pyr show strong adsorption with energies of -0.930 eV and -1.044 eV, respectively, indicating chemisorption. The substantial interaction energies suggest the formation of chemical bonds between pyridine molecules and the SiC surface, through charge transfer or orbital overlap. Functionalization of AHSiC with COOH and CHO groups alters the adsorption behavior. For AHSiC-s-COOH-Pyr, the E_a is -0.995 eV, suggesting chemisorption, but AHSiC-e-COOH-Pyr shows a much lower adsorption energy of -0.326 eV, indicating physisorption. The

Table 2

Mulliken charge values for C1, Si2, Si3, and the oxygen atom in the carbonyl (CO) group.

Compounds	C1	Si2	Si3	O of CO
AHSiC	-0.81	0.77	1.06	–
ZHSiC	-1.01	0.84	1.05	–
AHSiC-e-CHO	-0.70	0.82	1.09	-0.48
AHSiC-s-CHO	-0.81	0.78	1.08	-0.34
AHSiC-e-COOH	-0.72	0.83	1.06	-0.58
AHSiC-s-COOH	-0.80	0.78	1.27	-0.48
ZHSiC-e-CHO	-1.00	0.91	1.05	-0.36
ZHSiC-s-CHO	-1.01	0.84	1.06	-0.54
ZHSiC-e-COOH	-1.01	0.98	1.06	-0.39
ZHSiC-s-COOH	-1.01	0.84	1.07	-0.41

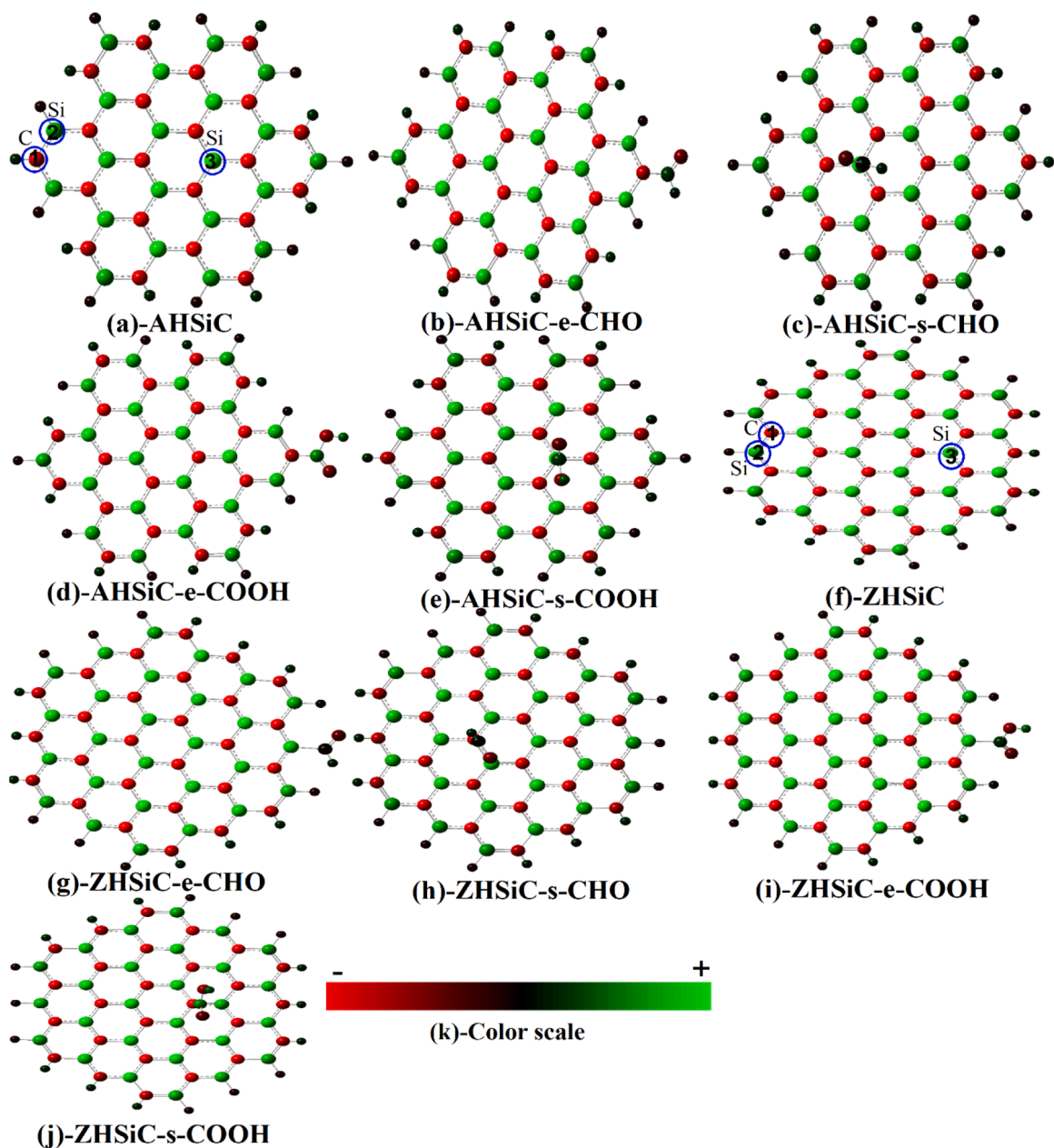


Fig. 3. (a–j) Mulliken charge distribution of AHSiC, ZHSiC, and their related materials. (j) displays the color scale, where red indicates regions of negative charge and green represents regions of positive charge.

weaker interaction for AHSiC-e-COOH-Pyr may result from steric hindrance or reduced affinity between pyridine and the functional group, which limits chemical bonding. CHO-functionalization leads to similarly varied results. AHSiC-s-CHO-Pyr has a strong chemisorption energy of -1.082 eV, while AHSiC-e-CHO-Pyr exhibits weaker adsorption at -0.514 eV, which is at the boundary between chemisorption and physisorption. The difference in adsorption strength between the s- and e-configurations can be attributed to structural factors that influence the extent of orbital overlap or charge transfer between the adsorbate and the surface.

For ZHSiC complexes, pristine surfaces exhibit strong chemisorption as well, with ZHSiC-s-Pyr having adsorption energy of -1.078 eV and ZHSiC-e-Pyr showing a weaker but still significant interaction of -0.553 eV. Functionalization with COOH strengthens adsorption for ZHSiC-s-COOH-Pyr, which has the highest adsorption energy of -1.284 eV, indicative of strong chemisorption. ZHSiC-e-COOH-Pyr also shows a strong chemisorptive interaction at -1.059 eV. This enhancement in adsorption energy for COOH-functionalized ZHSiC could be due to stronger electron-withdrawing effects of the COOH group, increasing the affinity for Pyr. CHO-functionalization shows a mixed adsorption behavior. ZHSiC-s-CHO-Pyr has weaker adsorption energy of -0.713 eV, indicating borderline chemisorption, while ZHSiC-e-CHO-Pyr shows stronger adsorption at -0.854 eV, suggesting chemisorption. The variation

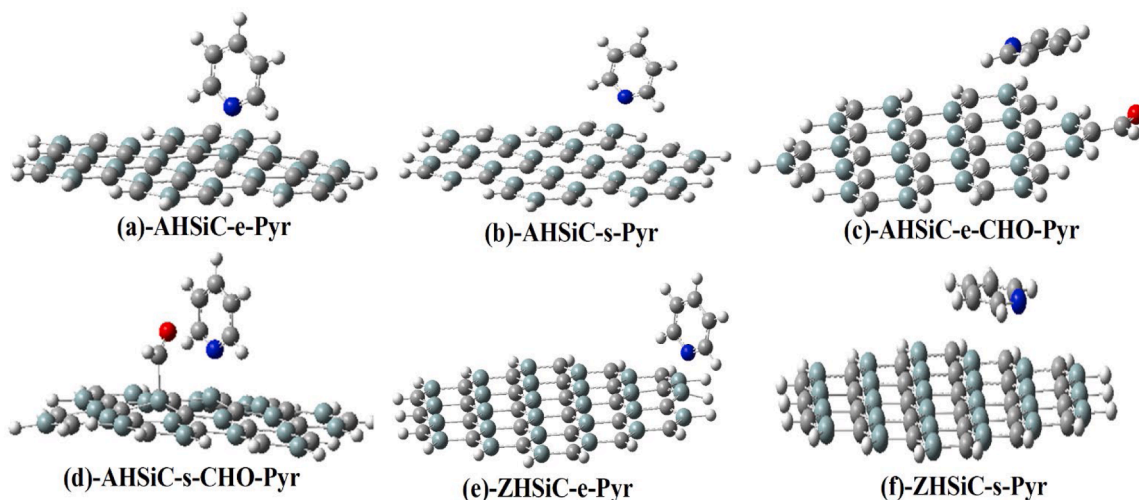


Fig. 4. Optimized structures of AHSiC, AHSiC-e-CHO, AHSiC-s-CHO, and ZHSiC after the adsorption of one Pyr-molecule at the edge and surface.

Table 3

Adsorption energy (E_a) and the recovery time (τ) of AHSiC, ZHSiC, as well as their functionalized derivatives, following the adsorption of a single pyridine molecule.

Complex	E_a (eV)	τ (s)	Complex	E_a (eV)	τ (s)
AHSiC-s-Pyr	-0.930	1.40×10^{-09}	AHSiC-e-COOH-Pyr	-0.326	1.26×10^{-11}
AHSiC-e-Pyr	-1.044	3.40×10^{-09}	AHSiC-s-COOH-Pyr	-0.995	2.31×10^{-09}
ZHSiC-s-Pyr	-1.078	4.42×10^{-09}	ZHSiC-e-CHO-Pyr	-0.854	7.71×10^{-10}
ZHSiC-e-Pyr	-0.553	7.40×10^{-11}	ZHSiC-s-CHO-Pyr	-0.713	2.57×10^{-10}
AHSiC-e-CHO-Pyr	-0.514	5.48×10^{-11}	ZHSiC-e-COOH-Pyr	-1.059	3.82×10^{-09}
AHSiC-s-CHO-Pyr	-1.082	4.55×10^{-09}	ZHSiC-s-COOH-Pyr	-1.284	2.20×10^{-08}

in adsorption strength between the s- and e-configurations can again be attributed to the different surface sites and their electronic properties, which affect how strongly pyridine interacts with the surface. In general, high adsorption energies observed in COOH-functionalized ZHSiC complexes and pristine surfaces can be attributed to stronger chemical bonding, driven by enhanced electronic interactions or favorable surface reactivity. Lower adsorption energies in e-functionalized complexes, especially with COOH and CHO, suggest physisorption due to weaker van der Waals forces or steric hindrance that limits the formation of chemical bonds. As shown in Figure S1, the E_a values vary significantly across different configurations of AHSiC and ZHSiC, as well as their functionalized derivatives. The highest E_a is observed for AHSiC functionalized with COOH at the edge site (AHSiC-e-COOH-Pyr), indicating strong chemisorption, which enhances the material's sensitivity for pyridine detection. Conversely, the lowest E_a is recorded for ZHSiC functionalized with COOH at the surface site (ZHSiC-s-COOH-Pyr), indicating weaker adsorption, which may contribute to faster recovery times.

3.2.2. Recovery time study

The recovery time (τ) of these complexes, as listed in Table 3, is critical in determining how easily pyridine desorbs from the surface after adsorption. For AHSiC, pristine surfaces have fast recovery time, with $\tau = 1.40 \times 10^{-9}$ s for AHSiC-s-Pyr and 3.40×10^{-9} s for AHSiC-e-Pyr. This suggests that despite strong chemisorption, the interaction is not irreversible, and pyridine can desorb quickly. Functionalization with COOH shows a varied impact. AHSiC-s-COOH-Pyr has a recovery time of 2.31×10^{-9} s, while AHSiC-e-COOH-Pyr shows a significantly faster recovery time of 1.26×10^{-11} s, suggesting that weaker physisorption facilitates rapid desorption in the e-configuration. CHO-functionalized complexes exhibit similar behavior, with AHSiC-s-CHO-Pyr recovering in 4.55×10^{-9} s and AHSiC-e-CHO-Pyr having a much faster desorption time of 5.48×10^{-11} s. For ZHSiC, pristine surfaces show slightly slower recovery times compared to AHSiC, with $\tau = 4.42 \times 10^{-9}$ s for ZHSiC-s-Pyr and 7.40×10^{-11} s for ZHSiC-e-Pyr. COOH-functionalized ZHSiC complexes have significantly longer recovery times, particularly ZHSiC-s-COOH-Pyr with the slowest recovery time of 2.20×10^{-8} s, indicating highly stable adsorption. ZHSiC-e-COOH-Pyr recovers more quickly at 3.82×10^{-9} s, while CHO-functionalized ZHSiC shows faster recovery times, with ZHSiC-s-CHO-Pyr at 2.57×10^{-10} s and ZHSiC-e-CHO-Pyr at 7.71×10^{-10} s. These results suggest that functionalization plays a key role in modulating recovery time, with COOH-functionalized ZHSiC, especially in the s-configuration, showing the slowest desorption, due to stronger chemisorptive interactions. Faster recovery times in e-configurations, particularly for AHSiC-e-COOH-Pyr, reflect weaker physisorption and easier desorption.

3.3. NBO study of pyridine adsorption

Table 4 presents the natural charge, population, and electronic configuration of nitrogen (N) in pyridine (Pyr) before and after adsorption onto AHSiC and ZHSiC, as well as their functionalized derivatives. This analysis provides insights into the electronic interactions and structural changes occurring during adsorption. The natural charge of N in Pyr before adsorption is -0.438 . After adsorption onto AHSiC, this charge becomes more negative, reaching -0.530 and -0.541 for AHSiC-s-Pyr and AHSiC-e-Pyr, respectively. This shift indicates that N in Pyr gains electron density from the SiC surface, suggesting a strong electron-donor-acceptor interaction that aligns with chemisorption. A similar trend is observed with ZHSiC, where N's charge increases to -0.446 for ZHSiC-s-Pyr and -0.540 for ZHSiC-e-Pyr. Natural population analysis shows that the total electron population of N in Pyr remains stable across all complexes, increasing slightly from 7.438 before adsorption to 7.530 for AHSiC-s-Pyr and 7.541 for AHSiC-e-Pyr. This stability suggests that N retains a similar overall electron density even after adsorption, although the valence and populations of Rydberg change subtly. The valence population increases after adsorption, indicating a shift in electron distribution towards the valence and Rydberg orbitals, with a minor increase in Rydberg contributions, reflecting minor orbital rearrangements. The electronic configuration reveals a shift primarily in the 2S and 2P orbitals. For example, in AHSiC-s-Pyr, the valence configuration shows 2S (1.33) and 2P (4.19), while in AHSiC-e-Pyr, the 2S and 2P populations are further enhanced, with 2S (1.33) and 2P (4.20). These changes suggest that orbital mixing occurs as pyridine interacts with the SiC surface, enhancing electron density in specific regions of the molecule's electronic structure.

Functionalization of AHSiC and ZHSiC affects the electronic characteristics of pyridine as well. For example, AHSiC-s-COOH-Pyr shows a charge of -0.502 , while AHSiC-e-COOH-Pyr's charge remains close to that of the pristine surface at -0.439 . This variation indicates that functionalization affects electron donation or withdrawal, influencing the electronic interaction between Pyr and the surface. Similar trends are observed with ZHSiC derivatives; for instance, ZHSiC-s-COOH-Pyr has a charge of -0.500 with a valence population of 5.486, showing slight electron donation from the surface. ZHSiC-e-COOH-Pyr has a more significant charge of -0.541 , reflecting stable configurations despite functionalization. Overall, the NBO analysis in Table 4 indicates that adsorption onto AHSiC and ZHSiC surfaces enhances electron density at N in pyridine, supporting the notion of chemisorption. The valence and Rydberg electron populations are altered upon adsorption, particularly in the 2S and 2P orbitals, highlighting how functionalization modulates charge distribution and electronic configuration. This effect underscores the potential of surface modifications to tailor adsorption properties.

3.4. Optical study

Fig. 5 (a-d) shows the calculated absorption spectra for AHSiC, ZHSiC, and their functionalized derivatives after the adsorption of a single pyridine molecule at the e- and s-sites. These spectra provide insights into the optical transitions, particularly the shifts in absorption peaks following adsorption and functionalization. Pyr adsorption induces a red shift in the absorption peaks, suggesting that electronic interactions between the SiC surfaces and pyr adjust the energy states, leading to lower transition energies. Functionalization with -CHO and -COOH groups further modulates these shifts, indicating that both the site of pyr adsorption and the type of functional group strongly influence the optical properties of these SiC systems.

Table 5 details the calculated excited states (ES), maximum wavelength (λ_{\max}), transition energy (TE), electronic transition (ET), oscillator strength (f), and transition coefficient (TC) for AHSiC, ZHSiC, and their functionalized derivatives upon pyr adsorption at the e and s sites. For pristine AHSiC, maximum wavelengths appear at 322 nm (ES 37) with a TE of 3.804 eV and 435 nm (ES 5) with a TE of 2.849 eV. The transition H-6 \rightarrow L+2 has a moderate oscillator strength ($f = 0.200$), while the H \rightarrow L transition is slightly stronger ($f = 0.165$), highlighting that transitions at lower energies tend to be more intense. ZHSiC shows λ_{\max} values at 340 nm (ES 42) and 493 nm (ES 4), with transitions of H-4 \rightarrow L+4 and H-1 \rightarrow L, respectively. The transition strength is particularly high for the H-1 \rightarrow L state ($f =$

Table 4

The natural charge, population, and electronic configuration for the N in Pyr were examined both before and after adsorption onto AHSiC, and ZHSiC, as well as their functionalized derivatives.

Compound	Charge	Natural population				Natural electronic configuration
		N of Pyr	Core	Valence	Rydberg	
Pyr	-0.438	1.999	5.428	0.011	7.438	[core]2S ^(1.39) 2p ^(4.04) 3p ^(0.01)
AHSiC-s-Pyr	-0.530	1.999	5.517	0.014	7.530	[core]2S ^(1.33) 2p ^(4.19) 3p ^(0.01)
AHSiC-e-Pyr	-0.541	1.999	5.528	0.014	7.541	[core]2S ^(1.33) 2p ^(4.20) 3p ^(0.01)
ZHSiC-s-Pyr	-0.446	1.999	5.436	0.011	7.446	[core]2S ^(1.39) 2p ^(4.05) 3p ^(0.01)
ZHSiC-e-Pyr	-0.540	1.999	5.527	0.014	7.540	[core]2S ^(1.32) 2p ^(4.20) 3p ^(0.01)
AHSiC-e-CHO-Pyr	-0.443	1.999	5.433	0.011	7.443	[core]2S ^(1.39) 2p ^(4.05) 3p ^(0.01)
AHSiC-s-CHO-Pyr	-0.544	1.999	5.531	0.014	7.544	[core]2S ^(1.32) 2p ^(4.21) 3p ^(0.01)
AHSiC-e-COOH-Pyr	-0.439	1.999	5.428	0.011	7.439	[core]2S ^(1.39) 2p ^(4.04) 3p ^(0.01)
AHSiC-s-COOH-Pyr	-0.502	1.999	5.488	0.015	7.502	[core]2S ^(1.36) 2p ^(4.13) 3p ^(0.01)
ZHSiC-e-CHO-Pyr	-0.537	1.999	5.524	0.014	7.537	[core]2S ^(1.33) 2p ^(4.19) 3p ^(0.01)
ZHSiC-s-CHO-Pyr	-0.464	1.999	5.453	0.011	7.464	[core]2S ^(1.39) 2p ^(4.07) 3p ^(0.01)
ZHSiC-e-COOH-Pyr	-0.541	1.999	5.528	0.014	7.541	[core]2S ^(1.33) 2p ^(4.20) 3p ^(0.01)
ZHSiC-s-COOH-Pyr	-0.500	1.999	5.486	0.015	7.500	[core]2S ^(1.35) 2p ^(4.14) 3p ^(0.01)

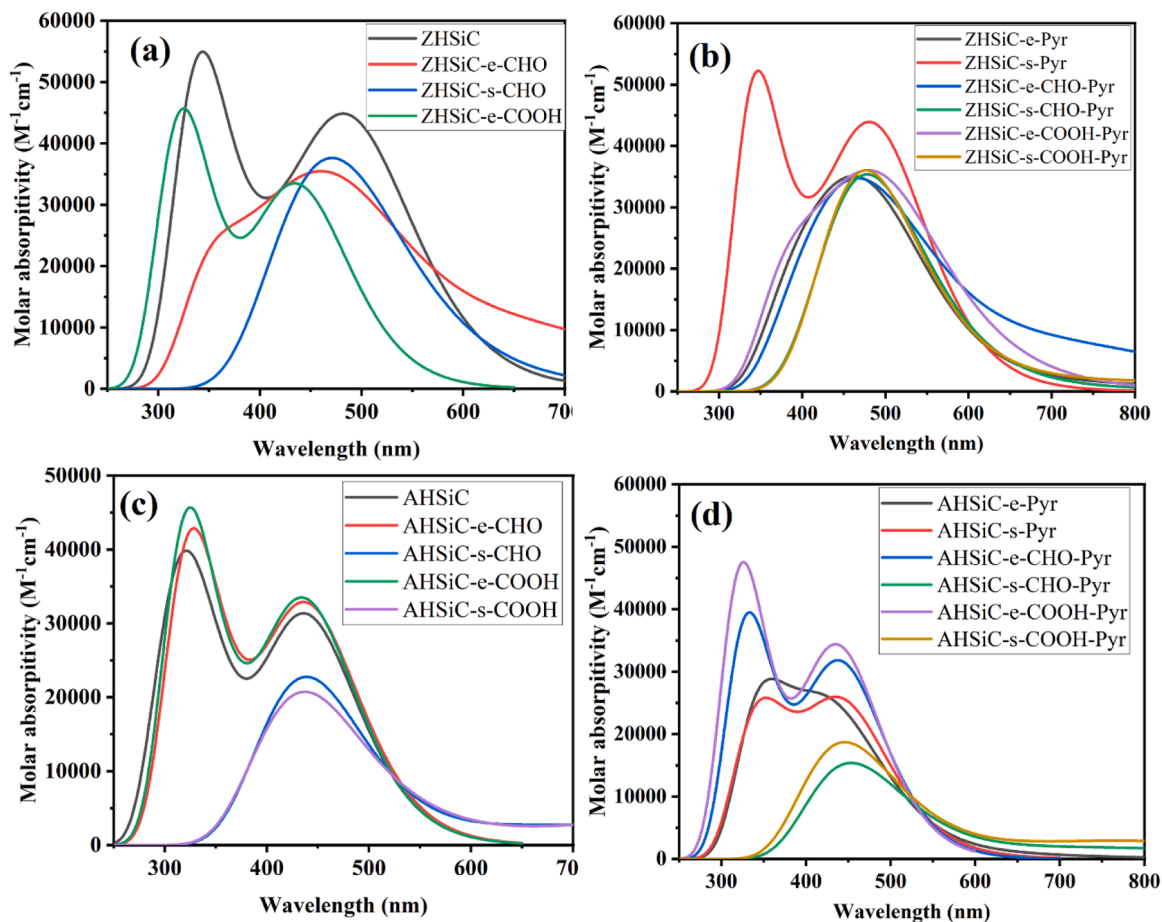


Fig. 5. (a-d) The calculated absorption spectra AHSiC, ZHSiC, as well as their functionalized derivatives, following the adsorption of a single pyridine molecule at both e and s sites.

0.425), indicating significant interaction between electronic states upon Pyr adsorption. Functionalized AHSiC and ZHSiC systems reveal additional shifts. For AHSiC functionalized with CHO at the e site, the λ_{\max} is 326 nm (TE = 3.799 eV, $f = 0.221$ for H-6→L) and 434 nm (TE = 2.854 eV, $f = 0.160$ for H-2→L). When CHO is functionalized at the s site, as in AHSiC-s-CHO, the maximum absorption shifts further to 438 nm (TE = 2.830 eV), with H→L+2 having a lower oscillator strength ($f = 0.090$). The CHO functionalization contributes to redshifts in absorption peaks, particularly at the s-site. The -COOH functionalization in AHSiC induces similar redshifts, as observed in AHSiC-e-COOH with maximum wavelengths at 325 nm and 434 nm. For AHSiC-s-COOH, the maximum wavelength appears at 437 nm (ES 31, TE = 2.835 eV, $f = 0.081$). Variations in oscillator strength across these states, particularly the lower values for surface functionalization, indicate that -COOH groups modify the electronic environment.

Upon adsorption of Pyr on functionalized AHSiC and ZHSiC, the absorption spectra exhibit additional shifts in maximum wavelengths. For AHSiC-e-CHO-Pyr, λ_{\max} appears at 334 nm (ES 36, TE = 3.710 eV) and 436 nm (ES 6, TE = 2.842 eV), with moderate oscillator strengths ($f = 0.230$ and $f = 0.207$). Pyr adsorption at the s-site, as in AHSiC-s-CHO-Pyr, causes a significant redshift, with λ_{\max} reaching 454 nm (ES 33, TE = 2.730 eV). For ZHSiC derivatives, Pyr adsorption at ZHSiC-e-CHO and ZHSiC-s-CHO sites results in absorption peaks at 455 nm and 468 nm, respectively, with enhanced oscillator strengths, particularly for ZHSiC-s-CHO-Pyr ($f = 0.250$). For ZHSiC functionalized with -COOH, redshifts are also observed, as in ZHSiC-e-COOH-Pyr with λ_{\max} at 479 nm and 343 nm, with strong transitions like H-1→L+1 and H-2→L+2, indicating enhanced electron-donor-acceptor interactions. Across these systems, the transitions primarily involve higher occupied (H-x) to lower unoccupied (L+y) orbitals, indicating increased electron interactions at specific energy levels following Pyr adsorption. The TC varies based on functionalization, such as AHSiC-s-CHO-Pyr (TC = 0.822) and ZHSiC-s-Pyr (TC = 0.670), indicating the influence of both adsorption sites and functional groups on electron transition intensities.

Overall, Fig. 5 and Table 5 illustrate that the adsorption of Pyr onto AHSiC and ZHSiC, combined with functionalization, results in a redshift in the absorption spectra, indicating strong electronic interactions. Functionalization with -CHO and -COOH groups further enhances these shifts, demonstrating the tunable optical and electronic properties of SiC surfaces through adsorption and functional modifications. The differences in oscillator strengths and transition coefficients highlight the impact of functional groups stabilizing certain electronic transitions, suggesting potential applications in optoelectronic devices that benefit from tailored electronic properties.

Table 5

The calculated excited state (ES), maximum wavelength (λ_{\max}), transition energy (TE), electronic transition (ET), oscillator strength (f), and transition coefficient (TC) of AHSiC, ZHSiC, as well as their functionalized derivatives, following the adsorption of a single pyridine molecule at both e and s sites.

Compounds	ES	$\lambda_{\max}(\text{nm})$	TE (eV)	ET	f	TC
AHSiC	37	322.000	3.804	H-6→L+2	0.200	0.353
	5	435.000	2.849	H→L	0.165	0.377
ZHSiC	42	340.000	3.580	H-4→L+4	0.523	0.414
	4	493.000	2.513	H-1→L	0.425	0.415
AHSiC-e-CHO	40	326.000	3.799	H-6→L	0.221	0.279
	6	434.000	2.854	H-2→L	0.160	0.416
AHSiC-s-CHO	31	438.000	2.830	H→L+2	0.090	0.405
AHSiC-e-COOH	37	325.000	3.691	H-8→L+1	0.260	0.341
	5	434.000	2.855	H→L+1	0.210	0.474
AHSiC-s-COOH	31	437.000	2.835	H-1→L+1	0.081	0.311
ZHSiC-e-CHO	10	455.000	2.725	H-1→L+2	0.251	0.575
ZHSiC-s-CHO	28	468.000	3.252	H-2→L+3	0.220	0.377
ZHSiC-e-COOH	43	343.000	3.607	H-4→L+4	0.360	0.294
	4	493.000	2.511	H-1→L+1	0.290	0.481
AHSiC-s-Pyr	37	351.000	3.529	H-3→L+4	0.140	0.528
	10	437.000	2.835	H-1→L+3	0.140	0.565
AHSiC-e-Pyr	31	361.000	3.430	H-4→L+3	0.180	0.325
	40	349.000	3.552	H-8→L	0.420	0.584
ZHSiC-s-Pyr	4	488.000	2.538	H-1→L+1	0.350	0.670
	13	457.000	2.711	H-6→L	0.250	0.673
AHSiC-e-CHO-Pyr	36	334.000	3.710	H-6→L+2	0.230	0.325
	6	436.000	2.842	H-1→L	0.207	0.363
AHSiC-s-CHO-Pyr	33	454.000	2.730	H-2→L+1	0.045	0.822
AHSiC-e-COOH-Pyr	39	324.000	3.822	H-6→L+2	0.308	0.396
	5	435.000	2.845	H-1→L	0.231	0.309
AHSiC-s-COOH-Pyr	30	445.000	2.780	H-1→L+1	0.090	0.116
ZHSiC-e-CHO-Pyr	16	468.000	2.644	H-1→3	0.180	0.446
ZHSiC-s-CHO-Pyr	23	481.000	2.577	H-6→L+2	0.250	0.466
ZHSiC-e-COOH-Pyr	10	479.000	2.587	H-2→L+2	0.220	0.398
ZHSiC-s-COOH-Pyr	26	478.000	2.589	H-1→L+2	0.250	0.398

3.5. Practical implications of functionalized SiC nanostructures in sensor applications

We analyzed the practical implications of functionalized AHSiC and ZHSiC nanostructures for sensor applications. The observed changes in the electronic and optical properties of these materials significantly improve sensor performance, leading to enhanced sensitivity, selectivity, and efficiency, making them promising candidates for various sensor applications. The functionalization of AHSiC and ZHSiC with CHO and COOH groups introduces surface charge density changes that lower the material's energy gap, facilitating easier electron transfer. This reduction in the energy gap enhances sensitivity, allowing the detection of trace concentrations of target molecules, such as pyridine, even in complex environments with background interference. In addition to these electronic improvements, functionalization alters the optical properties of both AHSiC and ZHSiC, including absorbance behavior. These changes enable non-invasive, extremely sensitive detection of adsorbed molecules through optical methods. Such characteristics make these functionalized materials ideal for applications like air quality monitoring, where real-time, non-invasive detection is essential. Furthermore, the ability to tailor the optical response for the selective molecule detection enhances their applicability in diverse sensor systems. However, there is a trade-off between strong adsorption (which increases sensitivity) and recovery time, which is crucial for sensor reusability. Strong chemisorption of pyridine molecules, particularly in COOH-functionalized ZHSiC, improves the sensor's ability to detect low concentrations of analytes but typically increases recovery time. This study shows that the functionalized SiC nanostructures achieve recovery times as low as 0.75 ns, striking a balance between strong adsorption and rapid recovery. This balance is essential for real-time, continuous sensor operation.

4. Conclusion

In conclusion, this research demonstrates that functionalizing AHSiC and ZHSiC with CHO and COOH groups significantly enhances their stability and modulates their electronic and optical properties. The functionalized materials exhibit strong adsorption capabilities, particularly for COOH-functionalized ZHSiC, and the recovery time of adsorbed molecules can be tuned by varying the functional group and adsorption site. These findings highlight the potential of functionalized SiC nanostructures for sensor applications that rely on optical properties and adsorption behavior. Future research should explore the adsorption of various analytes, optimize functionalization strategies, and integrate these materials into practical optical sensing devices.

CRedit authorship contribution statement

Nahed H. Teleb: Methodology. **Mahmoud A.S. Sakr:** Writing – review & editing, Writing – original draft. **Mohamed A. Saad:** Visualization. **Omar H. Abd-Elkader:** Investigation. **Hazem Abdelsalam:** Writing – review & editing, Conceptualization. **Qinfang Zhang:** Supervision.

Conflict of interest

The authors have declared no conflict of interest.

Acknowledgement

This work is supported by the National Natural Science Foundation of China (No. 12274361, No. 12474276). This work is also supported by Researchers Supporting Project number (RSP2025R468), King Saud University, Riyadh, Saudi Arabia.

Supplementary materials

Supplementary material associated with this article can be found, in the online version, at [doi:10.1016/j.cjph.2025.01.008](https://doi.org/10.1016/j.cjph.2025.01.008).

References

- [1] B.B. Campos, C. Abellán, M. Zougagh, J. Jimenez-Jimenez, E. Rodríguez-Castellón, J.C.G.E. Da Silva, A. Ríos, M. Algarra, Fluorescent chemosensor for pyridine based on N-doped carbon dots, *J. Coll. Interf. Sci.* 458 (2015) 209–216.
- [2] Y. Lv, Y. Zhang, Y. Du, J. Xu, J. Wang, A novel porphyrin-containing polyimide nanofibrous membrane for colorimetric and fluorometric detection of pyridine vapor, *Sensors* 13 (2013) 15758–15769.
- [3] Z. Li, J. Ma, Y. Zong, Y. Men, ZnS nanoparticles for high-sensitive fluorescent detection of pyridine compounds, *J. Alloys. Compd.* 559 (2013) 39–44.
- [4] C. Elosua, C. Barriain, I.R. Matias, A. Rodríguez, E. Colacio, A. Salinas-Castillo, A. Segura-Carretero, A. Fernandez-Gutiérrez, Pyridine vapors detection by an optical fibre sensor, *Sensors* 8 (2008) 847–859.
- [5] C. Elosua Aguado, C. Barriain Aisa, I. Matias Maestro, A. Rodríguez, E. Colacio, A. Salinas Castillo, A. Segura Carretero, A. Fernández Gutiérrez, Pyridine vapors detection by an optical fibre sensor, *Sensors* 8 (2) (2008) 847–859, 2008.
- [6] M.A. Farajzadeh, A. Yadeghari, H. Dehghani, S. Dastmalchi, Determination of pyridine as a decomposition product in ceftazidime and mouthwash solution, *Chromatographia* 80 (2017) 497–502.
- [7] J. Gopalakrishnan, S.A. Devi, Determination of triethylamine, pyridine and dimethyl formamide content in telmisartan by headspace gas chromatography using flame ionization detector, *Indian J. Pharm. Sci.* 78 (2016) 413–416.
- [8] S. Saha, R. Mistri, B.C. Ray, Determination of pyridine, 2-picoline, 4-picoline and quinoline from mainstream cigarette smoke by solid-phase extraction liquid chromatography/electrospray ionization tandem mass spectrometry, *J. Chromatogr. A* 1217 (2010) 307–311.
- [9] G. Pieraccini, S. Furlanetto, S. Orlandini, G. Bartolucci, I. Giannini, S. Pinzauti, G. Moneti, Identification and determination of mainstream and sidestream smoke components in different brands and types of cigarettes by means of solid-phase microextraction–gas chromatography–mass spectrometry, *J. Chromatogr. A* 1180 (2008) 138–150.
- [10] Y. Yamini, S. Seidi, A. Pourali, M. Rezaadeh, Electrical field-stimulated liquid-phase microextraction for trace analysis of pyridine and its derivatives in cigarette extract, *J. Iran. Chem. Soc.* 12 (2015) 503–511.
- [11] A.H. Kamel, M.E. Khalifa, S.A. Abd El-Maksoud, F.A. Elgendy, New plastic membrane sensors for selective determination of pyridine as a hazardous pollutant: validation and applications to flow injection analysis, *Int. J. Electrochem. Sci.* 9 (2014) 1663–1677.
- [12] S. Pirsá, N. Alizadeh, Rapid determination of pyridine derivatives by dispersive liquid–liquid microextraction coupled with gas chromatography/gas sensor based on nanostructured conducting polypyrrole, *Talanta* 87 (2011) 249–254.
- [13] K.L. Diehl, E.V. Anslын, Array sensing using optical methods for detection of chemical and biological hazards, *Chem. Soc. Rev.* 42 (2013) 8596–8611.
- [14] T.S. Vo, B. Jeon, T. Hoang, K.M. Lwin, S. Han, T.T.B.C. Vo, K. Kim, A comprehensive review of laser processing-assisted 2D functional materials and their specific applications, *Mater. Today Phys.* (2024) 101536.
- [15] G. Fiori, F. Bonaccorso, G. Iannaccone, T. Palacios, D. Neumaier, A. Seabaugh, S.K. Banerjee, L. Colombo, Electronics based on two-dimensional materials, *Nat. Nanotechnol.* 9 (2014) 768–779.
- [16] S.Z. Butler, S.M. Hollen, L. Cao, Y. Cui, J.A. Gupta, H.R. Gutiérrez, T.F. Heinz, S.S. Hong, J. Huang, A.F. Ismach, Progress, challenges, and opportunities in two-dimensional materials beyond graphene, *ACS Nano* 7 (2013) 2898–2926.
- [17] D. Akinwande, C.J. Brennan, J.S. Bunch, P. Egberts, J.R. Felts, H. Gao, R. Huang, J.-S. Kim, T. Li, Y. Li, A review on mechanics and mechanical properties of 2D materials—Graphene and beyond, *Extreme Mech. Lett.* 13 (2017) 42–77.
- [18] S. Kang, D. Lee, J. Kim, A. Capasso, H.S. Kang, J.-W. Park, C.-H. Lee, G.-H. Lee, 2D semiconducting materials for electronic and optoelectronic applications: potential and challenge, *2d Mater.* 7 (2020) 22003.
- [19] A.K. Geim, Graphene: status and prospects, *Science* (1979) 324 (2009) 1530–1534.
- [20] X. Ma, J. Yuan, Y. Mao, Accelerating the design and screening of surface-functionalized monolayer SiC for photocatalytic water splitting and ultraviolet applications via machine learning, *Mater. Today Chem.* 41 (2024) 102302.
- [21] I.J. Hernández-Hernández, F. de Santiago, A.L. Marcos-Viquez, Á. Miranda, M. Cruz-Irisson, L.A. Pérez, A comparative DFT study of CO and NO capture by copper- and titanium-functionalized SiC and GeC monolayers, *Mater. Lett.* (2024) 136805.
- [22] P. Vogt, P. De Padova, C. Quaresima, J. Avila, E. Frantzeskakis, M.C. Asensio, A. Resta, B. Ealet, G.L. Lay, Silicene: compelling experimental evidence for graphenelike two-dimensional silicon, *Phys. Rev. Lett.* 108 (2012) 155501.
- [23] S. Manzeli, D. Ovchinnikov, D. Pasquier, O.V. Yazyev, A. Kis, 2D transition metal dichalcogenides, *Nat. Rev. Mater.* 2 (2017) 1–15.
- [24] S. Subhan, M. Salman, M. Yaseen, MXenes as 2D inorganic materials: layered structures, modification, and characterization. MXenes as Emerging Modalities for Environmental and Sensing Applications, Elsevier, 2025, pp. 295–312.
- [25] M. Ali, H. Shi, F. Jan, S. Ahmed, Y. Song, E.-H. Han, A bifunctional self-healing coating enhanced by attapulgite functionalized MXene with inhibitor integration, *Prog. Org. Coat.* 199 (2025) 108936.
- [26] Y. Shi, Z. Du, S. Yang, A perspective of fabrication and applications of MXene–metal hybrids, *Adv. Funct. Mater.* 34 (2024) 2404653.
- [27] M. Naguib, M.W. Barsoum, Y. Gogotsi, Ten years of progress in the synthesis and development of MXenes, *Adv. Mater.* 33 (2021) 2103393.

- [28] S. Zhang, J. Yang, R. Xu, F. Wang, W. Li, M. Ghufraan, Y.-W. Zhang, Z. Yu, G. Zhang, Q. Qin, Extraordinary photoluminescence and strong temperature/angle-dependent Raman responses in few-layer phosphorene, *ACS Nano* 8 (2014) 9590–9596.
- [29] P.V. Pham, S.C. Bodepudi, K. Shehzad, Y. Liu, Y. Xu, B. Yu, X. Duan, 2D heterostructures for ubiquitous electronics and optoelectronics: principles, opportunities, and challenges, *Chem. Rev.* 122 (2022) 6514–6613.
- [30] S. Zeng, Z. Tang, C. Liu, P. Zhou, Electronics based on two-dimensional materials: status and outlook, *Nano Res.* 14 (2021) 1752–1767.
- [31] H. Abdelsalam, M.A.S. Sakr, N.H. Teleb, O.H. Abd-Elkader, W. Zhilong, Y. Liu, Q. Zhang, Highly efficient spin field-effect transistor based on nanographene and hBN heterostructures: spintronic and quantum transport properties, *Chin. J. Phys.* 90 (2024) 237–251.
- [32] Z. Liu, H.N. Alshareef, MXenes for optoelectronic devices, *Adv. Electron. Mater.* 7 (2021) 2100295.
- [33] E.C. Ahn, 2D materials for spintronic devices, *NPJ 2D Mater. Appl.* 4 (2020) 17.
- [34] H. Abdelsalam, O.H. Abd-Elkader, M.A.S. Sakr, N.H. Teleb, Y. Liu, Q. Zhang, Two-dimensional heterostars from nanographene and group-III nitrides for efficient spin filters: spintronic and quantum transport properties, *Results Phys.* 61 (2024) 107750.
- [35] X. Liu, M.C. Hersam, 2D materials for quantum information science, *Nat. Rev. Mater.* 4 (2019) 669–684.
- [36] C. Anichini, W. Czepa, D. Pakulski, A. Aliprandi, A. Ciesielski, P. Samorì, Chemical sensing with 2D materials, *Chem. Soc. Rev.* 47 (2018) 4860–4908.
- [37] G. Gao, A.P. O'Mullane, A. Du, 2D MXenes: a new family of promising catalysts for the hydrogen evolution reaction, *ACS Catal.* 7 (2017) 494–500.
- [38] H. Abdelsalam, M.M. Atta, W. Osman, Q. Zhang, Two-dimensional quantum dots for highly efficient heterojunction solar cells, *J. Coll. Interf. Sci.* 603 (2021) 48–57.
- [39] S. Suragtkhuu, S. Sunderiya, P. Myagmarsereejid, S. Purevdorj, A.S.R. Bati, B. Bold, Y.L. Zhong, S. Davaasambuu, M. Batmunkh, Graphene-like monoelemental 2D materials for perovskite solar cells, *Adv. Energy Mater.* 13 (2023) 2204074.
- [40] M. Shao, T. Bie, L. Yang, Y. Gao, X. Jin, F. He, N. Zheng, Y. Yu, X. Zhang, Over 21% efficiency stable 2D perovskite solar cells, *Adv. Mater.* 34 (2022) 2107211.
- [41] H. Abdelsalam, M.A.S. Sakr, G.M. Abdelrazek, N.H. Teleb, O.H. Abd-Elkader, Q. Zhang, 2D biphenylene-based nanostructures as prospective drug delivery carriers of carvedilol and levosim: DFT study, *Chem. Phys. Lett.* (2024) 141421.
- [42] H. Abdelsalam, Q.F. Zhang, Properties and applications of quantum dots derived from two-dimensional materials, *Adv. Phys. X* 7 (2022).
- [43] L. Tang, R. Ji, X. Li, K.S. Teng, S.P. Lau, Size-dependent structural and optical characteristics of glucose-derived graphene quantum dots, *Part. Part. Syst. Characteriz.* 30 (2013) 523–531.
- [44] Z.Z. Zhang, K. Chang, F.M. Peeters, Tuning of energy levels and optical properties of graphene quantum dots, *Phys. Rev. B* 77 (2008) 235411.
- [45] H. Abdelsalam, V.A. Saroka, M.M. Atta, W. Osman, Q. Zhang, Tunable electro-optical properties of doped chiral graphene nanoribbons, *Chem. Phys.* 544 (2021) 111116.
- [46] S. Kundu, V.K. Pillai, Synthesis and characterization of graphene quantum dots, *Phys. Sci. Rev.* 5 (2019) 20190013.
- [47] S. Kundu, R.M. Yadav, T.N. Narayanan, M.V. Shelke, R. Vajtai, P.M. Ajayan, V.K. Pillai, Synthesis of N, F and S co-doped graphene quantum dots, *Nanoscale* 7 (2015) 11515–11519.
- [48] J. Zhang, W. Xu, L. Wang, Z. Zheng, F. Liu, P. Yu, G. Yang, Colossal vacancy effect of 2D CuInP2S6 quantum dots for enhanced broadband photodetection, *Cryst. Growth Des.* (2023).
- [49] S.R. Ali, M. De, Defect-Engineered functionalized MoS2 quantum dots with enhanced antibacterial activity, *ACS Appl. Nano Mater.* (2023).
- [50] H. Abdelsalam, W.O. Younis, V.A. Saroka, N.H. Teleb, S. Yunoki, Q. Zhang, Interaction of hydrated metals with chemically modified hexagonal boron nitride quantum dots: wastewater treatment and water splitting, *Phys. Chem. Chem. Phys.* 22 (2020) 2566–2579.
- [51] C. Zhou, W. Jiang, B.K. Via, Facile synthesis of soluble graphene quantum dots and its improved property in detecting heavy metal ions, *Coll. Surf. B: Biointerf.* 118 (2014) 72–76.
- [52] H. Abdelsalam, N.H. Teleb, I.S. Yahia, H.Y. Zahran, H. Elhaes, M.A. Ibrahim, First principles study of the adsorption of hydrated heavy metals on graphene quantum dots, *J. Phys. Chem. Solids* 130 (2019) 32–40.
- [53] J. Prasongkit, V. Shukla, A. Grigoriev, R. Ahuja, V. Amornkitbamrung, Ultrahigh-sensitive gas sensors based on doped phosphorene: a first-principles investigation, *Appl. Surf. Sci.* 497 (2019) 143660.
- [54] H. Abdelsalam, V.A. Saroka, W.O. Younis, Phosphorene quantum dot electronic properties and gas sensing, *Phys. E: Low-Dimens. Syst. Nanostruct.* 107 (2019) 105–109.
- [55] K. Khan, A.K. Tareen, M. Iqbal, Z. Ye, Z. Xie, A. Mahmood, N. Mahmood, H. Zhang, Recent progress in emerging novel MXenes based materials and their fascinating sensing applications, *Small* (2023) 2206147.
- [56] H. Su, W. Wang, R. Shi, H. Tang, L. Sun, L. Wang, Q. Liu, T. Zhang, Recent advances in quantum dot catalysts for hydrogen evolution: synthesis, characterization, and photocatalytic application, *Carbon Energy* (2023) e280.
- [57] M.A.S. Sakr, M.A. Saad, Spectroscopic investigation, DFT, NBO and TD-DFT calculation for porphyrin (PP) and porphyrin-based materials (PPBMs), *J. Mol. Struct.* 1258 (2022) 132699.
- [58] M.J. Frisch, G.W. Trucks, H.B. Schlegel, G.E. Scuseria, M. Robb, J.R. Cheeseman, G. Scalmani, V. Barone, G.A. Petersson, H. Nakatsuji, Gaussian 16, Revision A. 03, 3, Gaussian, Inc., Wallingford CT, 2016.
- [59] K. Raghavachari, Perspective on “Density functional thermochemistry. III. The role of exact exchange” Becke AD (1993) *J Chem Phys* 98: 5648–52, *Theor. Chem. Acc.* 103 (2000) 361–363.
- [60] P.C. Hariharan, J.A. Pople, The influence of polarization functions on molecular orbital hydrogenation energies, *Theor. Chim. Acta* 28 (1973) 213–222.
- [61] Y. Ge, J. Ji, Q. Zhang, Z. Yuan, R. Wang, W. Zhang, S. Sang, Unraveling the intrinsic magnetic property of triangular zigzag edge bilayer graphene nanoflakes: a first-principles theoretical study, *Chem. Phys. Lett.* 730 (2019) 326–331.
- [62] H. Abdelsalam, M. Ali, N.H. Teleb, M.M. Ibrahim, M.A. Ibrahim, Q. Zhang, Two-dimensional Si2BN nanoflakes for efficient removal of heavy metals, *Chem. Phys. Lett.* 772 (2021) 138568.
- [63] H. Abdelsalam, M.A.S. Sakr, V.A. Saroka, O.H. Abd-Elkader, Q. Zhang, Nanoporous graphene quantum dots constructed from nanoribbon superlattices with controllable pore morphology and size for wastewater treatment, *Surf. Interf.* (2023) 103109.